

Interpreting Object-level Foundation Models via Visual Precision Search

Ruoyu Chen^{1,2}, Siyuan Liang³, Jingzhi Li^{1,2}, Shiming Liu⁴, Maosen Li⁵,
Zheng Huang⁶, Hua Zhang^{1,2}, and Xiaochun Cao⁷

¹Institute of Information Engineering, Chinese Academy of Sciences, Beijing 100093, China

²School of Cyber Security, University of Chinese Academy of Sciences, Beijing 100049, China

³School of Computing, National University of Singapore, 119077, Singapore

⁴RAMS Lab, Huawei Technologies Co., Ltd. ⁵IAS BU, Huawei Technologies Co., Ltd.

⁶College of Computer, National University of Defense Technology

⁷School of Cyber Science and Technology, Shenzhen Campus of Sun Yat-sen University

chenruoyu@iie.ac.cn caoxiaochun@mail.sysu.edu.cn

Abstract

Advances in multimodal pre-training have propelled object-level foundation models, such as Grounding DINO and Florence-2, in tasks like visual grounding and object detection. However, interpreting these models' decisions has grown increasingly challenging. Existing interpretable attribution methods for object-level task interpretation have notable limitations: (1) gradient-based methods lack precise localization due to visual-textual fusion in foundation models, and (2) perturbation-based methods produce noisy saliency maps, limiting fine-grained interpretability. To address these, we propose a Visual Precision Search method that generates accurate attribution maps with fewer regions. Our method bypasses internal model parameters to overcome attribution issues from multimodal fusion, dividing inputs into sparse sub-regions and using consistency and collaboration scores to accurately identify critical decision-making regions. We also conducted a theoretical analysis of the boundary guarantees and scope of applicability of our method. Experiments on RefCOCO, MS COCO, and LVIS show our approach enhances object-level task interpretability over SOTA for Grounding DINO and Florence-2 across various evaluation metrics, with faithfulness gains of 23.7%, 31.6%, and 20.1% on MS COCO, LVIS, and RefCOCO for Grounding DINO, and 102.9% and 66.9% on MS COCO and RefCOCO for Florence-2. Additionally, our method can interpret failures in visual grounding and object detection tasks, surpassing existing methods across multiple evaluation metrics. The code will be released at <https://github.com/RuoyuChen10/VPS>.

1. Introduction

Understanding object information in images, such as object detection [6, 13, 23, 51, 52, 57], is a crucial and endur-

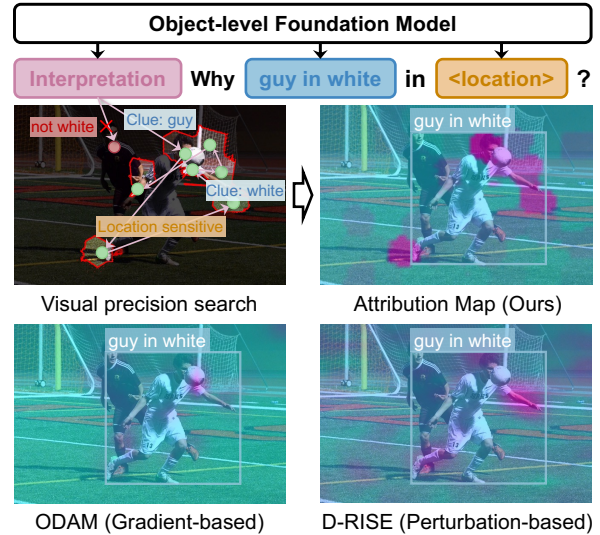


Figure 1. Illustration of our Visual Precision Search interpretation method, which more precisely identifies key sub-regions in object-level foundation model decision-making compared to gradient-based and perturbation-based methods.

ing challenge in computer vision, holding significant importance across various fields, including autonomous driving [3, 14, 45]. With advancements in multimodal alignment technology [19, 34], object-level foundation models [27, 47, 49, 56] like Grounding DINO [27] and Florence-2 [49] have been developed to handle various tasks, including visual grounding and object detection. However, the massive data volume, rich semantic concepts, and large parameters significantly reduce the transparency [20, 21, 25] and interpretability [4, 10, 55] of these models. Since object-level tasks like autonomous driving demand high model reliability [8, 29, 46], building transparent and interpretable models is crucial for enhancing safety and trustworthy [5, 16, 20, 22, 23, 44], making it essential to inter-

pret object-level foundation models.

Some interpretable attribution algorithms for traditional object detection models have been proposed, including gradient-based methods like ODAM [54] and perturbation-based methods like D-RISE [33]. However, as shown in the lower panel of Figure 1, these methods face limitations when applied to multimodal foundation models: (1) gradient-based methods may struggle to provide accurate visual localization explanations due to the fusion of visual and textual features in foundation models, and (2) perturbation-based approaches can introduce sampling artifacts, resulting in noisy saliency maps with limited fine-grained interpretability.

To address these issues, we propose a novel interpretation mechanism for the object-level foundation model, as shown in Figure 1. Our goal is to generate a saliency map that explains the rationale behind the model’s detection of a specific object, allowing fewer regions to be exposed for accurate detection. Additionally, removing these critical regions should quickly lead to detection failure, highlighting their importance in the model’s decision. Specifically, we propose Visual Precision Search, which sparsifies the input region into a series of sub-regions using super-pixel segmentation, and then ranks these sparse sub-regions to determine their importance for object-level decision-making. Our gradient-free method *circumvents localization errors at the visual level that are caused by gradient back-propagation in vision-text fusion*. Furthermore, we propose a novel submodular function, grounded in theoretical analysis and offering boundary guarantees for Visual Precision Search. This function identifies regions that enhance interpretability from two key perspectives: clues that support the model’s accurate detection and regions with strong combinatorial effects. By employing region search to iteratively expand the set of sub-regions, our method more precisely identifies key sub-regions in the decision-making of object-level foundation models, which *mitigates the issue of coarse explanations caused by noise in perturbation-based methods*. In addition, our method effectively analyzes cases of grounding or detection failure, allowing us to observe which input-level factors influence the decision.

We validated our method on the MS COCO [24], RefCOCO [17], and LVIS [12] datasets. The object-level foundation models evaluated include Grounding DINO, which uses a multimodal feature fusion architecture, and Florence-2, which employs a multimodal large language model architecture. The tasks covered include interpreting visual grounding and object detection. In explaining the data behind correct model decisions, our method demonstrates that the faithfulness metric for Grounding DINO surpasses SOTA method D-RISE by 23.7%, 20.1%, and 31.6% on MS COCO, RefCOCO, and LVIS, respectively. For Florence-2, our method improves the faithfulness metric by 102.9%

and 66.9% on MS COCO and RefCOCO, respectively, while also achieving SOTA performance on location metrics across all datasets. In interpreting the factors leading to Grounding DINO’s failures in visual grounding tasks, our method improves the Insertion metric by 42.9% and the average highest score by 25.1%. It also identifies causes of detector misclassification and undetection, achieving Insertion metric improvements of 54.7% and 42.7% for misclassification, and 36.7% and 64.3% for undetection on MS COCO and LVIS, respectively.

In summary, the contributions of this paper are:

- We introduce Visual Precision Search, a new search-based mechanism for interpreting object-level foundation models through instance-specific saliency maps.
- A novel submodular mechanism is constructed to enhance interpretability from two aspects: identifying clues that support accurate detection and highlighting regions with strong combinatorial effects, with an analysis of its theoretical boundaries for object-level tasks.
- We demonstrate our approach’s generalizability across multimodal foundation models, including both non-LLM-based (Grounding DINO) and LLM-based detectors (Florence-2).
- We validate our method on MS COCO, RefCOCO, and LVIS, achieving significant improvements in explaining object-level tasks. Additionally, we analyze grounding and detection failures, establishing a quantitative benchmark for this purpose.

2. Related Work

Object Detection. Object detection involves locating objects in images and identifying their categories [23]. Early models typically used convolutional neural network (CNN) backbones, divided into two main types: two-stage and single-stage models. Two-stage methods, like Faster R-CNN [36] and Mask R-CNN [13], generate region proposals to identify potential foreground objects before refining localization and classification. In contrast, single-stage methods, such as YOLO [42] and FCOS [40], directly classify and regress on backbone features. Transformer architectures [41] have further advanced object detection, as exemplified by DETR [2], which uses a fully end-to-end Transformer-based approach. The rise of multimodal foundation models [19, 34] has enabled open-set detection tasks [23], allowing object grounding with textual input [6, 48]. GLIP [19] frames detection as a grounding problem, integrating vision and language through feature fusion in the neck module. Grounding DINO [27] uses multi-phase vision-language fusion, achieving state-of-the-art (SOTA) referring expression comprehension (REC) [26]. Other methods explore multimodal large language models (MLLMs) for detection and grounding tasks. Florence-2 [49], for instance, introduces a prompt-based model

that generates object categories and coordinates using text prompts directly. The diverse feature extractors, architectures, and outputs in object detection make it challenging to interpret their decisions using a single unified approach.

Object Detection Explanation. Explaining object detector decisions remains a largely unexplored area. Gudovskiy *et al.* [11] used Integrated Gradients (IG) [39] and SHAP [37] with SSD [28] classification scores for box-level attribution. Lee *et al.* [18] optimized masks on Mask R-CNN [13] to approximate original decisions with minimal pixels. Petsiuk *et al.* [33] proposed D-RISE, an adaptation of RISE [32], though it often introduces noise in saliency maps. Jiang *et al.* [15] introduced Nesterov-Accelerated iGOS++, which can be resource-intensive for large models. Zhao *et al.* [54] developed ODAM using Grad-CAM [38], but its effectiveness depends on network layer choices. SSGrad-CAM++ [50] focuses on minimizing unrelated regions in saliency maps. While these methods aim to interpret detector errors, they largely rely on simple visualizations and empirical observations, often overlooking input-level feature confusion that can obscure human understanding. Masking confusing regions may aid in correcting model outputs [5]. Our paper introduces a black-box interpretation approach for object-level foundation models using Visual Precision Search, enhancing detection performance with fewer regions and identifying input-level failure causes to improve detection accuracy.

3. Method

This section presents our method for explaining the decisions of object-level foundation models. Specifically, Section 3.1 outlines the basic concepts and problem formulation. Section 3.2 details the construction of our proposed Visual Precision Search interpretation method, and Section 3.3 provides the theoretical analysis. Figure 2 illustrates the overall framework of our method.

3.1. Problem Formulation

Given an image $\mathbf{I} \in \mathbb{R}^{h \times w \times 3}$ and an object-level foundation model $f(\cdot)$, the output can be represented as $f(\mathbf{I}) = \{(\mathbf{b}_i, c_i, s_i) \mid i = 1, 2, \dots, N\}$. Each tuple (\mathbf{b}_i, c_i, s_i) denotes the bounding box, class label, and confidence score for each detected object i , where N is the maximum number of detection boxes. Tasks like object detection involve multiple boxes and categories, while visual grounding tasks like referring expression comprehension (REC) have only one box and category. Our goal is to generate a saliency map that explains the reasons behind the model’s detection of a specific object, (\mathbf{b}_i, c_i, s_i) . Ideally, this explanation would enable the correct detection of objects using fewer input regions, while also requiring the removal of only a few critical regions to invalidate the detector. To achieve this, we can sparsify the input region $V = \{\mathbf{I}_1^s, \dots, \mathbf{I}_m^s\}$,

where \mathbf{I}_i^s represents the i -th sub-region, m is the total number of sub-regions, and $\mathbf{I} = \sum_{i=1}^m \mathbf{I}_i^s$. We then frame the saliency map generation task as a subset selection problem for these input sub-regions. A set function $\mathcal{F}(\cdot)$ is defined to assess interpretability by determining whether a given region is a key factor in the model’s decision. Therefore, the objectives are:

$$\max_{S \subseteq V, |S| < k} \mathcal{F}(S), \quad (1)$$

where k denotes the maximum number of sub-regions. Therefore, the key to this problem lies in designing set function \mathcal{F} and optimizing Eq. 1.

3.2. Visual Precision Search

We propose a Visual Precision Search method for interpreting object-level models. To begin, the input region needs to be sparsified. We apply the SLICO superpixel segmentation algorithm [1] to divide the input into m sub-regions, $V = \{\mathbf{I}_1^s, \dots, \mathbf{I}_m^s\}$. To solve Eq. 1, an \mathcal{NP} -hard problem, we employ submodular optimization [9]. Since the saliency map requires all sub-regions to be ranked, k can be set to $|V|$ to compute ordered subsets. When the set function $\mathcal{F}(\cdot)$ satisfies the properties of diminishing returns¹ and monotonic non-negative², a greedy search guarantees an approximate optimal solution [7], with $\mathcal{F}(S) \geq (1 - 1/e)\mathcal{F}(S^*)$, where S^* denotes the optimal solution and S denotes the greedy solution. We next design a set function to evaluate the interpretability score and rank the importance of interpretable regions for object-level tasks.

Clue Score: An essential aspect of interpretability is enabling the object-level foundation model to accurately locate and identify objects while using fewer regions. To assess the importance of subregions from this perspective, we introduce the object location box information, $\mathbf{b}_{\text{target}}$, and the target category, c , that requires explanation. Given a subregion S , the object-level model outputs N instances, denoted as $f(S) = \{(\mathbf{b}_i, s_{c,i}) \mid i = 1, \dots, N\}$, where $s_{c,i}$ represents the confidence of the i -th bounding box in predicting category c . Then, the clue score of sub-region S is defined as:

$$s_{\text{clue}}(S, \mathbf{b}_{\text{target}}, c) = \max_{(\mathbf{b}_i, s_{c,i}) \in f(S)} \text{IoU}(\mathbf{b}_{\text{target}}, \mathbf{b}_i) \cdot s_{c,i}, \quad (2)$$

where $\text{IoU}(\cdot, \cdot)$ represents the Intersection over Union between two bounding boxes. Unlike Petsiuk *et al.* [33], which only considers high-confidence bounding boxes, our method includes all candidate boxes to avoid getting stuck in a local optimum during the search. By incorporating the clue score s_{clue} , our method focuses on regions that strengthen the desired positional and semantic response.

¹Diminishing returns: $\forall S_A \subseteq S_B \subseteq V \setminus \alpha, \mathcal{F}(S_A \cup \{\alpha\}) - \mathcal{F}(S_A) \geq \mathcal{F}(S_B \cup \{\alpha\}) - \mathcal{F}(S_B)$.

²Monotonic non-negative: $\forall S \subseteq V \setminus \alpha, \mathcal{F}(S \cup \{\alpha\}) - \mathcal{F}(S) \geq 0$.

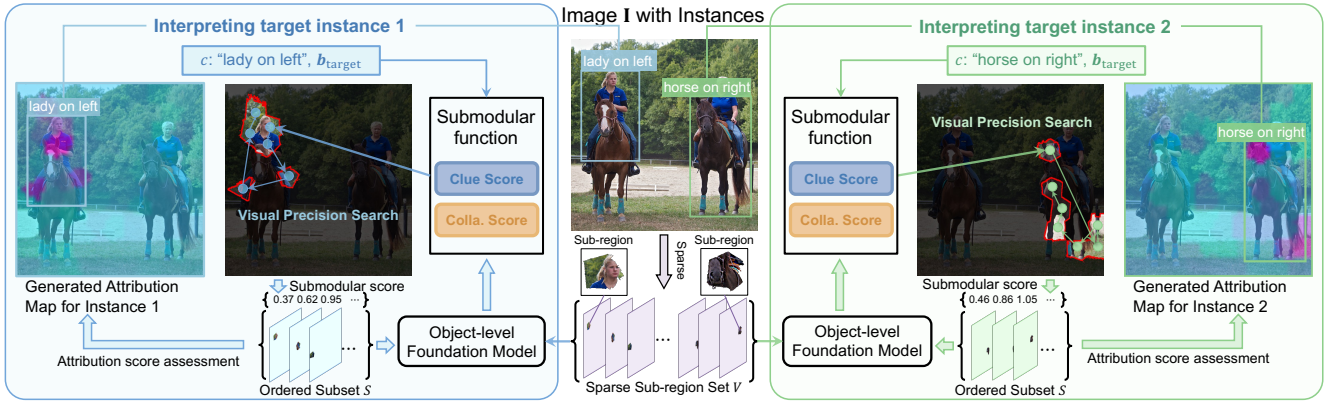


Figure 2. Framework of the proposed Visual Precision Search method for interpreting an object-level foundation model. The input is first sparsified into a set of sub-regions and then interpreted across different instances. A submodular function guides the search for significant sub-regions, updating the ordered subset iteratively, and ultimately generating the instance-level attribution map.

Collaboration Score: Some regions may exhibit strong combination effects, meaning they contribute effectively to model decisions only when paired with multiple specific sub-regions. Therefore, we introduce the collaboration score s_{colla} to assess sub-regions with high sensitivity to decision outcomes:

$$s_{\text{colla}}(S, \mathbf{b}_{\text{target}}, c) = 1 - \max_{(\mathbf{b}_i, s_{c,i}) \in f(V \setminus S)} \text{IoU}(\mathbf{b}_{\text{target}}, \mathbf{b}_i) \cdot s_{c,i}, \quad (3)$$

this means that no detection box can accurately or confidently locate the object once the key sub-region is removed. This score serves as an effective guide in the initial search phase to identify subtle key regions that contribute to the final decision.

Submodular Function: The scores above are combined to construct a submodular function $\mathcal{F}(\cdot)$, as follows:

$$\mathcal{F}(S, \mathbf{b}_{\text{target}}, c) = s_{\text{clue}}(S, \mathbf{b}_{\text{target}}, c) + s_{\text{colla}}(S, \mathbf{b}_{\text{target}}, c). \quad (4)$$

Saliency Map Generation: Using the above submodular function, a greedy search algorithm is applied to sort all sub-regions in V , yielding an ordered subset S . Introducing the submodular function enables the search algorithm to more precisely identify key visual regions for interpretation. Additionally, scoring the sub-regions is necessary to better explain the importance of each sub-region. We evaluate the salient difference between the two sub-regions by the marginal effect. The attribution score \mathcal{A}_i for each sub-region s_i in S is assessed by:

$$\mathcal{A}_i = \begin{cases} b_{\text{base}} & \text{if } i = 1, \\ \mathcal{A}_{i-1} - |\mathcal{F}(S_{[i]}) - \mathcal{F}(S_{[i-1]})| & \text{if } i > 1, \end{cases} \quad (5)$$

where b_{base} represents a baseline attribution score for the first sub-region, and $S_{[i]}$ denotes the set containing the top i sub-regions in S . When a new sub-region is added, a small marginal increase suggests comparable importance to the previous sub-region. A negative marginal effect indicates a counterproductive impact, which can be assessed by its absolute value. Finally, \mathcal{A} is normalized to obtain the saliency map of the sub-region. The detailed calculation process of

the proposed Visual Precision Search algorithm is outlined in Algorithm 1.

Algorithm 1: Visual Precision Search algorithm for generating interpretable saliency maps of object-level foundation models.

Input: Image $\mathbf{I} \in \mathbb{R}^{h \times w \times 3}$, a division algorithm $\text{Div}(\cdot)$, the object location box $\mathbf{b}_{\text{target}}$, and the target category c .

Output: An ordered set S and a saliency map $\mathcal{A} \in \mathbb{R}^{h \times w}$.

```

1  $V \leftarrow \text{Div}(\mathbf{I})$ ;
2  $S \leftarrow \emptyset$ ; /* Initiate the operation of
   submodular subset selection */
3  $\mathcal{A}_1 \leftarrow b_{\text{base}}$ ;
4 for  $i = 1$  to  $|V|$  do
5    $S_d \leftarrow V \setminus S$ ;
6    $\alpha \leftarrow \arg \max_{\alpha \in S_d} \mathcal{F}(S \cup \{\alpha\}, \mathbf{b}_{\text{target}}, c)$ ;
7    $S \leftarrow S \cup \{\alpha\}$ ;
8   if  $i > 1$  then
9      $\mathcal{A}_i \leftarrow \mathcal{A}_{i-1} - |\mathcal{F}(S_{[i]}) - \mathcal{F}(S_{[i-1]})|$ 
10 end
11 return  $S, \text{norm}(\mathcal{A})$ 

```

3.3. Theory Analysis

A theoretical analysis is conducted for our Visual Precision Search method. We analyze the designed set function, and the applicability of the proposed method.

Theorem 1 (Submodular Properties). *Consider two subsets S_A and S_B in set V , where $S_A \subseteq S_B \subseteq V$. Given an element α , where $\alpha \in V \setminus S_B$. Assuming that α is contributing to model interpretation, then, the function $\mathcal{F}(\cdot)$ in Eq. 4 satisfies diminishing returns,*

$$\mathcal{F}(S_A \cup \{\alpha\}) - \mathcal{F}(S_A) \geq \mathcal{F}(S_B \cup \{\alpha\}) - \mathcal{F}(S_B),$$

and monotonic non-negative, $\mathcal{F}(S_A \cup \{\alpha\}) - \mathcal{F}(S) \geq 0$, and thus, \mathcal{F} is a submodular function.

Proof. Please see supplementary material for the proof. \square

Remark 1 (Impact on Sparse Division). *The quality of the search space is determined by sparse division, meaning that both the method of partitioning the input and the number*

of sub-regions play a crucial role in the faithfulness of the Visual Precision Search.

Remark 2 (Applicable Models). *If the model provides bounding box positions and category confidence without filtering out low-confidence detection boxes, the interpretation results of the Visual Precision Search can achieve guaranteed optimal boundaries. Models with detection heads are generally applicable; however, MLLM-based models may not directly output confidence scores, leaving room for improvement in the interpretation results.*

4. Experiments

This section validates our interpretation method for object-level foundation models. Section 4.1 covers the experimental setup, followed by evaluation metrics in Section 4.2. Section 4.3 shows our approach’s faithfulness in explaining correct decisions, and Section 4.4 assesses its ability to identify factors behind errors. Finally, Section 4.5 analyzes the ablation study results.

4.1. Experimental Setup

Datasets. We evaluate the proposed method on three object-level datasets: MS COCO 2017 [24], LVIS V1 [12], and RefCOCO [17]. The MS COCO dataset, used for interpreting object detection with 80 classes, involves random sampling of 5 correctly detected (IoU > 0.5, correct category), 3 misclassified (IoU > 0.5, wrong category), and 3 undetected (IoU < 0.5 or low confidence) instances per class. The LVIS V1 dataset, with 1,203 categories including 337 rare ones (1–10 images), uses Grounding DINO for interpreting zero-shot detection on rare classes, analyzing 165 correctly detected, 152 misclassified, and 534 undetected samples. The RefCOCO dataset, for interpreting referring expression comprehension (REC), evaluates 500 correctly grounded (IoU > 0.5) and 200 incorrectly grounded (IoU < 0.5) samples per model.

Baselines. The interpretation methods we compare include gradient-based approaches: Grad-CAM [38], SSGrad-CAM++[50], and ODAM[54], as well as perturbation-based methods: D-RISE [33] and D-HSIC [31]. D-RISE and D-HSIC are allowed to use all model outputs, including low-confidence detection boxes, to enhance the sufficiency of saliency estimation.

Implementation Details. We validate our method on two object-level foundation models, Grounding DINO³ [27] and Florence-2⁴ [49], across object detection and referring expression comprehension (REC) tasks. To interpret model decisions, we set the ground truth bounding box and category as target box $\mathbf{b}_{\text{target}}$ and category c . By default, the

SLICO superpixel segmentation algorithm divides the image into 100 sparse sub-regions.

4.2. Evaluation Metrics

Faithfulness Metrics. We evaluate the faithfulness of interpretation results across the entire image using Insertion and Deletion scores from the detection task, following the setup by Petsiuk *et al.* [33]. These metrics reflect location and recognition accuracy. We also calculate classification and IoU scores for the box closest to the target explanation denoted as Insertion (class), Deletion (class), Insertion (IoU), and Deletion (IoU). Additionally, we compute the average highest confidence, defined as the highest class response for the box closest to the target with IoU > 0.5. For failure samples, we introduce the Explaining Successful Rate (ESR) to evaluate whether the saliency map can effectively guide the search within a limited region, enabling the model to correctly detect misclassified or low-confidence objects (with IoU > 0.5 and classification confidence above the detector’s default threshold) previously.

Location Metrics. We report the Point Game [53] and Energy Point Game [43] metrics. Since these metrics typically assume that the model’s decision is relevant to the target object [33], we calculate them only for interpretation results on samples the model has correctly detected.

4.3. Faithfulness Analysis

4.3.1. Faithfulness on Grounding DINO

We begin by validating our approach in explaining decisions across various object-level tasks using Grounding DINO [27]. Table 1 presents the faithfulness results across different datasets and tasks, demonstrating the strong interpretative faithfulness of our method.

In the object detection interpretation task on the MS COCO dataset, our method achieved state-of-the-art results, outperforming the D-RISE method by 23.7% on the Insertion metric, 6.7% on the Deletion metric, and 10.6% on the average highest score. The Insertion and Deletion metrics also achieved top performance under both category and IoU conditions. Additionally, our method performed best in location metrics, indicating state-of-the-art performance in explaining general object detection tasks. We also found that gradient-based methods, such as ODAM, exhibit low faithfulness in explaining Grounding DINO decisions. This is primarily due to the fusion of text and visual modalities, which causes the gradient to be influenced by both, reducing its effectiveness in attributing to the visual modality alone.

In the referring expression comprehension (REC) interpretation task on the RefCOCO dataset, our method achieved state-of-the-art results across all evaluation metrics, surpassing the D-RISE method by 20.1% on the Insertion metric, 22.1% on the Deletion metric, and 4.4% on the average highest score. These results confirm that our

³<https://github.com/IDEA-Research/GroundingDINO>

⁴<https://huggingface.co/microsoft/Florence-2-large-ft>

Table 1. Evaluation of faithfulness metrics (Deletion, Insertion AUC scores, and average highest score) and location metrics (Point Game and Energy Point Game) on the MS-COCO, RefCOCO, and LVIS V1 (rare) validation sets for correctly detected or grounded samples using Grounding DINO.

Datasets	Methods	Faithfulness Metrics							Location Metrics	
		Ins. (↑)	Del. (↓)	Ins. (class) (↑)	Del. (class) (↓)	Ins. (IoU) (↑)	Del. (IoU) (↓)	Ave. high. score (↑)	Point Game (↑)	Energy PG (↑)
MS COCO [24] (Detection task)	Grad-CAM [38]	0.2436	0.1526	0.3064	0.2006	0.6229	0.5324	0.5904	0.1746	0.1463
	SSGrad-CAM++ [50]	0.2107	0.1778	0.2639	0.2314	0.5981	0.5511	0.5886	0.1905	0.1293
	D-RISE [33]	0.4412	0.0402	0.5081	0.0886	0.8396	0.3642	0.6215	0.9497	0.1850
	D-HSIC [31]	0.3776	0.0439	0.4382	0.0903	0.8301	0.3301	0.5862	0.7328	0.1861
	ODAM [54]	0.3103	0.0519	0.3655	0.0894	0.7869	0.3984	0.5865	0.5431	0.2034
Ours	0.5459	0.0375	0.6204	0.0882	0.8581	0.3300	0.6873	0.9894	0.2046	
RefCOCO [17] (REC task)	Grad-CAM [38]	0.3749	0.4237	0.4658	0.5194	0.7516	0.7685	0.7481	0.2380	0.2171
	SSGrad-CAM++ [50]	0.4113	0.3925	0.5008	0.4851	0.7700	0.7588	0.7561	0.2820	0.2262
	D-RISE [33]	0.6178	0.1605	0.7033	0.3396	0.8606	0.5164	0.8471	0.9400	0.2870
	D-HSIC [31]	0.5491	0.1846	0.6295	0.3509	0.8504	0.5120	0.7739	0.7900	0.3190
	ODAM [54]	0.4778	0.2718	0.5620	0.3757	0.8217	0.6641	0.7425	0.6320	0.3529
Ours	0.7419	0.1250	0.8080	0.2457	0.9050	0.5103	0.8842	0.9460	0.3566	
LVIS V1 (rare) [12] (Zero-shot det. task)	Grad-CAM [38]	0.1253	0.1294	0.1801	0.1814	0.5657	0.5910	0.3549	0.1151	0.0941
	SSGrad-CAM++ [50]	0.1253	0.1254	0.1765	0.1775	0.5800	0.5691	0.3504	0.1091	0.0931
	D-RISE [33]	0.2808	0.0289	0.3348	0.0835	0.8303	0.3174	0.4289	0.9697	0.1462
	D-HSIC [31]	0.2417	0.0353	0.2912	0.0928	0.8187	0.3550	0.4044	0.8303	0.1730
	ODAM [54]	0.2009	0.0410	0.2478	0.0844	0.7760	0.4082	0.3694	0.6061	0.2050
Ours	0.3695	0.0277	0.4275	0.0799	0.8479	0.3242	0.4969	0.9758	0.1785	

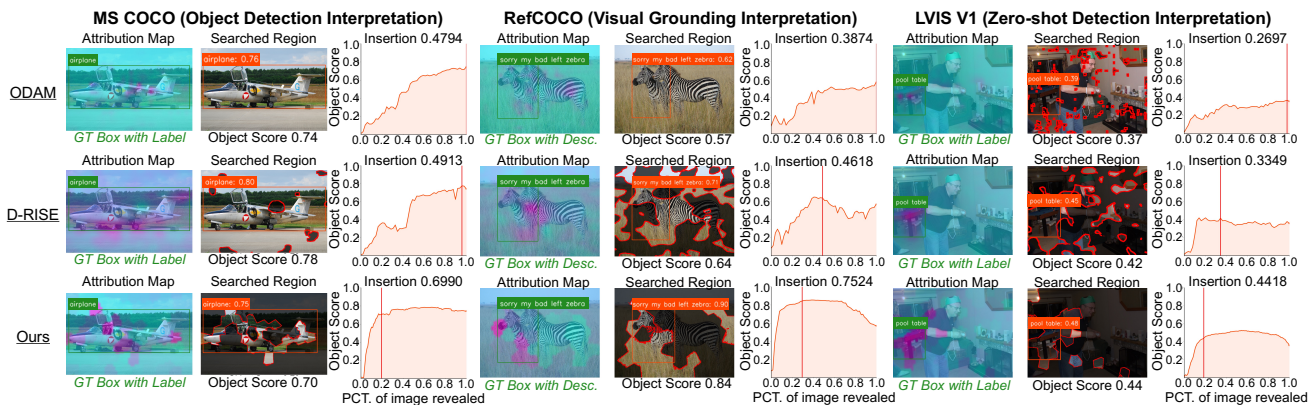


Figure 3. Visualization results of Grounding DINO for interpreting object localization tasks on the MS COCO, RefCOCO, and LVIS V1 datasets. The first column shows the saliency map with the ground truth box and label. The second column presents detection within the limited search region, and the third columns display the insertion curves.

method maintains high faithfulness in explaining object description understanding.

We also interpret zero-shot object detection for rare classes on the LVIS V1 dataset. Our method achieved SOTA results in faithfulness metrics, surpassing D-RISE by 31.6% on the Insertion metric, 4.2% on the Deletion metric, and 15.9% on the average highest score. Although our method ranks second to ODAM on Energy Point Game metrics, this is mainly due to Grounding DINO not being fully trained on rare LVIS classes; as a result, model responses may be influenced by other regions rather than the object.

Experimental results show that our method significantly outperforms other interpretability approaches, primarily due to the submodularity of our objective function, enabling precise evaluation of critical sub-regions. As shown in Figure 3, ODAM’s saliency maps are diffuse, and D-RISE’s maps are noisy, whereas our method sharply highlights essential sub-regions, capturing edges and class-specific features that enhance interpretability.

4.3.2. Faithfulness on Florence-2

We further validated our approach on Florence-2 [49], a foundation model lacking object confidence scores. This

limitation requires our search to rely solely on IoU as a guiding metric, excluding comparison with gradient-based methods. As shown in Table 2, our method achieves state-of-the-art performance.

In the object detection interpretability task on the MS COCO dataset, our method outperforms D-RISE by 3.8% on the Insertion metric and achieves a substantial improvement of 102.9% on the Deletion metric. Additionally, our method enhances the Point Game and Energy Point Game metrics by 8.3% and 60.7%, respectively. Due to the absence of object confidence scores in Florence-2, it becomes challenging to identify areas that quickly invalidate the model’s detection results. Compared to perturbation-based methods, our approach offers significant advantages; it relies more directly on the object itself, resulting in stronger faithfulness to the model’s detection behavior.

We also interpret referring expression comprehension (REC) interpretation task on the RefCOCO dataset, outperforming D-RISE by 6.1% and 66.9% in Insertion and Deletion metrics, respectively. Our approach also achieved state-of-the-art localization results, with a 14.6% improvement in the Energy Point Game, demonstrating strong interpretability.

Table 2. Evaluation of faithfulness metrics (Deletion and Insertion AUC scores) and location metrics (Point Game and Energy Point Game) on the MS COCO and RefCOCO validation sets for correctly detected and grounded samples using Florence-2.

Datasets	Methods	Faithfulness Metrics		Location Metrics	
		Insertion (\uparrow)	Deletion (\downarrow)	Point Game (\uparrow)	Energy PG (\uparrow)
MS COCO [24] (Detection task)	D-RISE [33]	0.7477	0.0972	0.8850	0.1568
	D-HSIC [31]	0.5345	0.2730	0.2925	0.0862
	Ours	0.7759	0.0479	0.9583	0.2519
RefCOCO [17] (REC task)	D-RISE [33]	0.7922	0.3505	0.8480	0.2464
	D-HSIC [31]	0.7639	0.3560	0.6980	0.2754
	Ours	0.8409	0.1159	0.8660	0.3927

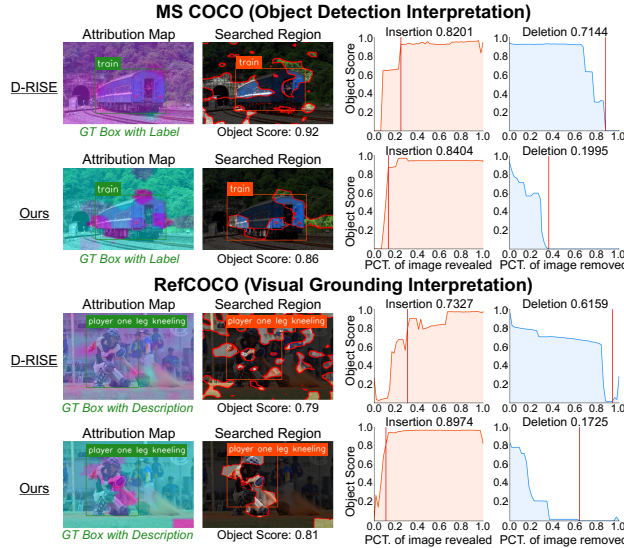


Figure 4. Visualization results of Florence-2 for interpreting object localization tasks on the MS COCO and RefCOCO datasets.

ity in accurately pinpointing object information.

We visualized some results of our method in Figure 4, illustrating that it effectively identifies key information about the object’s location and categorical description. While D-RISE performed well on the Insertion metric, its attribution results were diffuse and lacked reliability, and it did not perform as well on the Deletion metric.

4.4. Interpreting Failures in Object-Level Tasks

4.4.1. Interpreting REC Failures

Failures in the REC task primarily arise from visual grounding errors, often due to interference from other objects in the scene that become entangled with the text. Removing this distracting visual information can clarify grounding results and improve error understanding at the visual input level. To achieve this, we specify the correct location as the target box, denoted as b_{target} , for input attribution. Table 3 shows the attribution results, where gradient-based methods exhibit limited performance in faithfulness metrics. Compared to D-RISE, our approach improves Insertion by 42.9%, class score-based Insertion by 25.1%, and average highest score by 14.9%. Figure 5 illustrates model error interpretations, with the cyan-highlighted region indicating decision errors due to visual input interference that leads the foundation model astray.

Table 3. Insertion AUC scores and the average highest score on the RefCOCO validation sets for or the samples with incorrect localization in visual grounding using Grounding DINO.

Datasets	Methods	Faithfulness Metrics		
		Ins. (\uparrow)	Ins. (class) (\uparrow)	Ave. high. score (\uparrow)
RefCOCO [17] (REC task)	Grad-CAM [38]	0.1536	0.2794	0.3295
	SSGrad-CAM++ [50]	0.1590	0.2837	0.3266
	D-RISE [33]	0.3486	0.4787	0.6096
	D-HSIC [31]	0.2274	0.3488	0.4495
	ODAM [54]	0.1793	0.3001	0.3453
Ours	0.4981	0.5990	0.7007	

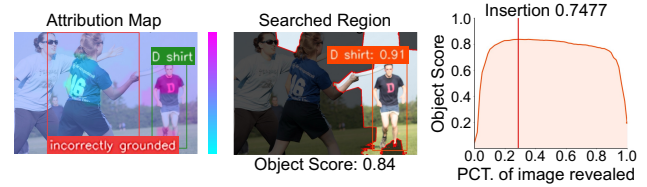


Figure 5. Visualization of the method for discovering what causes the Grounding DINO incorrectly grounded on RefCOCO.

Table 4. Insertion AUC scores, average highest score, and explaining successful rate (ESR) on the MS-COCO and the LVIS validation sets for misclassified samples using Grounding DINO.

Datasets	Methods	Faithfulness Metrics			
		Ins. (\uparrow)	Ins. (class) (\uparrow)	Ave. high. score (\uparrow)	ESR (\uparrow)
MS COCO [24] (Detection task)	Grad-CAM [38]	0.1091	0.1478	0.3102	38.38%
	SSGrad-CAM++ [50]	0.0960	0.1336	0.2952	33.51%
	D-RISE [33]	0.2170	0.2661	0.3603	50.26%
	D-HSIC [31]	0.1771	0.2161	0.3143	34.59%
	ODAM [54]	0.1129	0.1486	0.2869	32.97%
Ours	0.3357	0.3967	0.4591	69.73%	
LVIS V1 (rare) [12] (Zero-shot det. task)	Grad-CAM [38]	0.0503	0.0891	0.1564	12.50%
	SSGrad-CAM++ [50]	0.0574	0.0946	0.1580	11.84%
	D-RISE [33]	0.1245	0.1647	0.2088	28.95%
	D-HSIC [31]	0.0963	0.1247	0.1748	16.45%
	ODAM [54]	0.0575	0.0954	0.1520	9.21%
Ours	0.1776	0.2190	0.2606	53.29%	

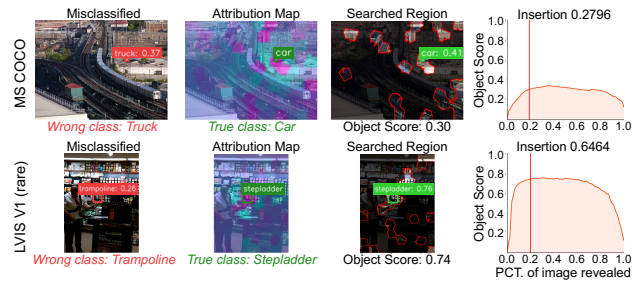


Figure 6. Visualization of our method reveals the causes of Grounding DINO misclassifications on MS COCO and LVIS. The cyan region in the saliency map highlights the regions responsible for the model’s misclassification.

4.4.2. Interpreting Detection Failures

Detection failures include misclassification and undetected objects. While previous works [33, 54] used visualization to explain errors, it lacked quantitative analysis, resulting in lower trustworthiness. We used saliency maps to identify input-level interference causing detection failures.

Misclassified Interpretation. As shown in Table 4, On the MS COCO dataset, our method outperforms D-RISE, improving Insertion by 54.7%, Insertion (class) by 49.1%, average highest score by 27.4%, and explaining success rate (ESR) by 19.47%. Similarly, on the LVIS dataset, our method shows advantages with improvements of 42.7% in Insertion, 33.0% in Insertion (class), 24.8% in average highest score, and 24.34% in ESR. This improvement is pri-

Table 5. Insertion, average highest score, and explaining successful rate (ESR) on the MS-COCO and the LVIS V1 (rare) validation sets for missed detection samples using Grounding DINO.

Datasets	Methods	Faithfulness Metrics			
		Ins. (↑)	Ins. (class) (↑)	Ave. high. score (↑)	ESR (↑)
MS COCO [24] (Detection task)	Grad-CAM [38]	0.0760	0.1321	0.2153	16.44%
	SSGrad-CAM++ [50]	0.0671	0.1151	0.2124	16.44%
	D-RISE [33]	0.1538	0.2260	0.2564	26.94%
	D-HSIC [31]	0.1101	0.1716	0.1945	13.56%
	ODAM [54]	0.0745	0.1350	0.2037	13.78%
	Ours	0.2102	0.3011	0.3014	41.33%
LVIS V1 (rare) [12] (Zero-shot det. task)	Grad-CAM [38]	0.0291	0.0689	0.0901	5.43%
	SSGrad-CAM++ [50]	0.0292	0.0680	0.0897	5.24%
	D-RISE [33]	0.0703	0.1184	0.1312	18.73%
	D-HSIC [31]	0.0516	0.0920	0.1168	13.48%
	ODAM [54]	0.0283	0.0716	0.0851	4.68%
	Ours	0.1155	0.1886	0.1784	30.15%

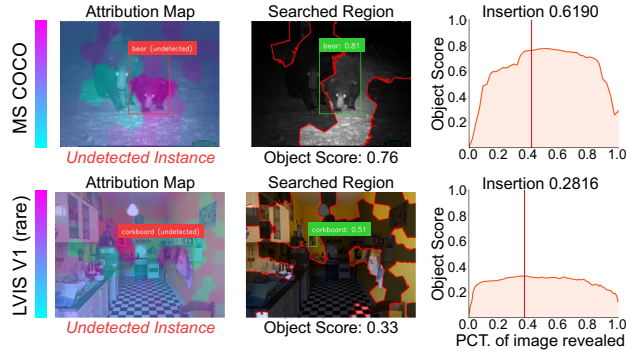


Figure 7. Visualization of our method reveals the causes of Grounding DINO undetected on MS COCO and LVIS. The cyan region in the saliency map highlights the regions responsible for the model’s detection failure.

marily due to our proposed Visual Precision Search, which confines attribution to the target negative response region, effectively refining the model’s detection results. Figure 6 shows that the background surrounding the object interferes with the model’s decision-making. Improving the model by refining the contextual relationship between foreground and background may be a promising direction.

Undetected Interpretation. Low object confidence may result from both the model’s feature representation and confounding input-level factors. We analyze causes of missed detections, with Table 5 showing that our method achieves SOTA performance across metrics. On MS COCO, it outperforms D-RISE with a 36.7% improvement in Insertion and a 14.39% gain in ESR, while on LVIS, it improves Insertion by 64.3% and ESR by 11.42%. Figure 7 visualizes our method’s explanations for undetected instances, revealing that errors may arise from challenges in distinguishing similar objects (e.g., the bear in the first row) and environmental influence on detection (e.g., the corkboard in the second row). These insights highlight current model limitations, offering directions for improvement.

4.5. Ablation Study

We conduct ablation studies on the proposed Visual Precision Search algorithm, focusing on two key aspects: the submodular function and the number of sub-regions.

Ablation of the Submodular Function. We analyze the effectiveness of our submodular function design on

Table 6. Ablation study on function score components for Grounding DINO on the MS COCO validation set.

Clue Score (Eq. 2)	Colla. Score (Eq. 3)	Faithfulness Metrics		
		Insertion (↑)	Deletion (↓)	Ave. high. score (↑)
✓	✓	0.3632	0.0378	0.5967
✓	✗	0.5370	0.0799	0.6864
✓	✓	0.5459	0.0375	0.6873

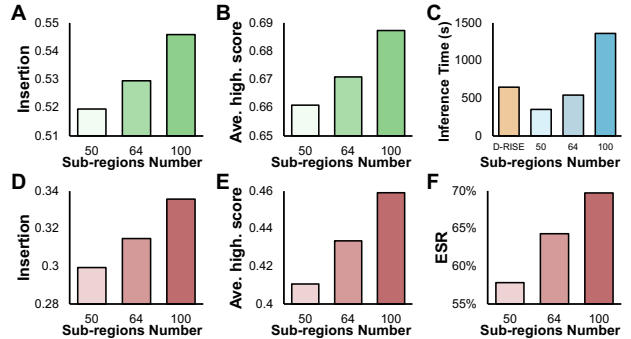


Figure 8. Ablation on the number of sub-regions. For correct detections, panels A and B show the effect of sub-region count on Insertion and average highest score, respectively. Panel C presents the inference time for different sub-region counts. For misclassified samples, panels D, E, and F display the effects on Insertion, average highest score, and explanation success rate.

Grounding DINO using correctly detected samples from MS COCO. Table 6 shows the results. The Clue Score identifies regions beneficial for detection, improving Insertion and average highest score, while the Collaboration Score pinpoints sensitive regions, enhancing the Deletion metric by causing the detector to fail more quickly. Combining these scores enables our method to achieve optimal results across indicators, demonstrating the effectiveness of each score function within the submodular function.

Ablation on Divided Sub-region Number. The sub-region number affects search space quality. Using Grounding DINO, we assess its impact on correctly predicted and misclassified samples in MS COCO. Figures 8A-B show that when the model predicts correctly, increasing the number of sub-regions leads to higher Insertion and average highest scores, indicating that finer divisions enhance the faithfulness of search results. Additionally, Figures 8D-F show that, for misclassified samples, Insertion, average highest score, and ESR also improve as the number of sub-regions increases. Figure 8C shows inference times for our search algorithm on an RTX 3090 compared to D-RISE across various subregion counts. Increasing sub-regions improves faithfulness but also rapidly increases inference time. Future work will aim to increase subregion count and inference speed without sacrificing attribution performance.

5. Conclusion

In this paper, we propose an interpretable attribution method specifically tailored for object-level foundation models, called the Visual Precision Search method, which introduces a novel submodular mechanism that combines a clue score and a collaboration score. This method achieves

enhanced interpretability with fewer search regions. Experiments on RefCOCO, MS COCO, and LVIS demonstrate that our approach improves object-level task interpretability over state-of-the-art methods for Grounding DINO and Florence-2 across various evaluation metrics. Furthermore, our method effectively interprets failures in visual grounding and object detection tasks.

References

- [1] Radhakrishna Achanta, Appu Shaji, Kevin Smith, Aurelien Lucchi, Pascal Fua, and Sabine Süsstrunk. SLIC superpixels compared to state-of-the-art superpixel methods. *IEEE Trans. Pattern Anal. Mach. Intell.*, 34(11):2274–2282, 2012. [3](#)
- [2] Nicolas Carion, Francisco Massa, Gabriel Synnaeve, Nicolas Usunier, Alexander Kirillov, and Sergey Zagoruyko. End-to-end object detection with transformers. In *Eur. Conf. Comput. Vis. (ECCV)*, pages 213–229, 2020. [2](#)
- [3] Li Chen, Penghao Wu, Kashyap Chitta, Bernhard Jaeger, Andreas Geiger, and Hongyang Li. End-to-end autonomous driving: Challenges and frontiers. *IEEE Trans. Pattern Anal. Mach. Intell.*, 2024. [1](#)
- [4] Ruoyu Chen, Jingzhi Li, Hua Zhang, Changchong Sheng, Li Liu, and Xiaochun Cao. Sim2Word: Explaining similarity with representative attribute words via counterfactual explanations. *ACM Trans. Multim. Comput. Commun. Appl.*, 19(6):1–22, 2023. [1](#)
- [5] Ruoyu Chen, Hua Zhang, Siyuan Liang, Jingzhi Li, and Xiaochun Cao. Less is more: Fewer interpretable region via submodular subset selection. In *Int. Conf. Learn. Represent. (ICLR)*, 2024. [1, 3](#)
- [6] Tianheng Cheng, Lin Song, Yixiao Ge, Wenyu Liu, Xinggang Wang, and Ying Shan. Yolo-world: Real-time open-vocabulary object detection. In *IEEE Conf. Comput. Vis. Pattern Recog. (CVPR)*, pages 16901–16911, 2024. [1, 2](#)
- [7] Jack Edmonds. Submodular functions, matroids, and certain polyhedra. *Combinatorial Structures and Their Applications*, pages 69–87, 1970. [3](#)
- [8] Di Feng, Ali Harakeh, Steven L Waslander, and Klaus Dietmayer. A review and comparative study on probabilistic object detection in autonomous driving. *IEEE Transactions on Intelligent Transportation Systems*, 23(8):9961–9980, 2021. [1](#)
- [9] Satoru Fujishige. *Submodular functions and optimization*. Elsevier, 2005. [3, 12](#)
- [10] Yossi Gandelsman, Alexei A Efros, and Jacob Steinhardt. Interpreting clip’s image representation via text-based decomposition. In *Int. Conf. Learn. Represent. (ICLR)*, 2024. [1](#)
- [11] Denis Gudovskiy, Alec Hodgkinson, Takuya Yamaguchi, Yasunori Ishii, and Sotaro Tsukizawa. Explain to fix: A framework to interpret and correct dnn object detector predictions. *arXiv preprint arXiv:1811.08011*, 2018. [3](#)
- [12] Agrim Gupta, Piotr Dollar, and Ross Girshick. LVIS: A dataset for large vocabulary instance segmentation. In *IEEE Conf. Comput. Vis. Pattern Recog. (CVPR)*, pages 5356–5364, 2019. [2, 5, 6, 7, 8](#)
- [13] Kaiming He, Georgia Gkioxari, Piotr Dollár, and Ross Girshick. Mask R-CNN. *IEEE Trans. Pattern Anal. Mach. Intell.*, 42(2):386–397, 2018. [1, 2, 3, 12](#)
- [14] Yihan Hu, Jiazhi Yang, Li Chen, Keyu Li, Chonghao Sima, Xizhou Zhu, Siqi Chai, Senyao Du, Tianwei Lin, Wenhai Wang, et al. Planning-oriented autonomous driving. In *IEEE Conf. Comput. Vis. Pattern Recog. (CVPR)*, pages 17853–17862, 2023. [1](#)
- [15] Mingqi Jiang, Saeed Khorram, and Fuxin Li. Diverse explanations for object detectors with nesterov-accelerated igos++. In *Brit. Mach. Vis. Conf. (BMVC)*, pages 188–189, 2023. [3](#)
- [16] Mingqi Jiang, Saeed Khorram, and Li Fuxin. Comparing the decision-making mechanisms by transformers and cnns via explanation methods. In *IEEE Conf. Comput. Vis. Pattern Recog. (CVPR)*, pages 9546–9555, 2024. [1](#)
- [17] Sahar Kazemzadeh, Vicente Ordonez, Mark Matten, and Tamara Berg. ReferItGame: Referring to objects in photographs of natural scenes. In *Proc. Conf. Empir. Methods Nat. Lang. Process. (EMNLP)*, pages 787–798, 2014. [2, 5, 6, 7](#)
- [18] Jungbeom Lee, Jihun Yi, Chaehun Shin, and Sungroh Yoon. BBAM: Bounding box attribution map for weakly supervised semantic and instance segmentation. In *IEEE Conf. Comput. Vis. Pattern Recog. (CVPR)*, pages 2643–2652, 2021. [3](#)
- [19] Liunian Harold Li, Pengchuan Zhang, Haotian Zhang, Jianwei Yang, Chunyuan Li, Yiwu Zhong, Lijuan Wang, Lu Yuan, Lei Zhang, Jenq-Neng Hwang, et al. Grounded language-image pre-training. In *IEEE Conf. Comput. Vis. Pattern Recog. (CVPR)*, pages 10965–10975, 2022. [1, 2](#)
- [20] Siyuan Liang, Baoyuan Wu, Yanbo Fan, Xingxing Wei, and Xiaochun Cao. Parallel rectangle flip attack: A query-based black-box attack against object detection. In *Int. Conf. Comput. Vis. (ICCV)*, pages 7697–7707, 2021. [1](#)
- [21] Siyuan Liang, Longkang Li, Yanbo Fan, Xiaojun Jia, Jingzhi Li, Baoyuan Wu, and Xiaochun Cao. A large-scale multiple-objective method for black-box attack against object detection. In *Eur. Conf. Comput. Vis. (ECCV)*, pages 619–636, 2022. [1](#)
- [22] Siyuan Liang, Aishan Liu, Jiawei Liang, Longkang Li, Yang Bai, and Xiaochun Cao. Imitated detectors: Stealing knowledge of black-box object detectors. In *ACM Int. Conf. Multimedia*, pages 4839–4847, 2022. [1](#)
- [23] Siyuan Liang, Wei Wang, Ruoyu Chen, Aishan Liu, Boxi Wu, Ee-Chien Chang, Xiaochun Cao, and Dacheng Tao. Object detectors in the open environment: Challenges, solutions, and outlook. *arXiv preprint arXiv:2403.16271*, 2024. [1, 2](#)
- [24] Tsung-Yi Lin, Michael Maire, Serge Belongie, James Hays, Pietro Perona, Deva Ramanan, Piotr Dollár, and C Lawrence Zitnick. Microsoft COCO: Common objects in context. In *Eur. Conf. Comput. Vis. (ECCV)*, pages 740–755, 2014. [2, 5, 6, 7, 8](#)
- [25] Aishan Liu, Jun Guo, Jiakai Wang, Siyuan Liang, Renshuai Tao, Wenbo Zhou, Cong Liu, Xianglong Liu, and Dacheng Tao. {X-Adv}: Physical adversarial object attacks against

- x-ray prohibited item detection. In *USENIX Security Symposium*, pages 3781–3798, 2023. 1
- [26] Jingyu Liu, Liang Wang, and Ming-Hsuan Yang. Referring expression generation and comprehension via attributes. In *Int. Conf. Comput. Vis. (ICCV)*, pages 4856–4864, 2017. 2
- [27] Shilong Liu, Zhaoyang Zeng, Tianhe Ren, Feng Li, Hao Zhang, Jie Yang, Chunyuan Li, Jianwei Yang, Hang Su, Jun Zhu, et al. Grounding DINO: Marrying dino with grounded pre-training for open-set object detection. In *Eur. Conf. Comput. Vis. (ECCV)*, 2024. 1, 2, 5
- [28] Wei Liu, Dragomir Anguelov, Dumitru Erhan, Christian Szegedy, Scott Reed, Cheng-Yang Fu, and Alexander C Berg. SSD: Single shot multibox detector. In *Eur. Conf. Comput. Vis. (ECCV)*, pages 21–37, 2016. 3, 12
- [29] Dimity Miller, Feras Dayoub, Michael Milford, and Niko Sünderhauf. Evaluating merging strategies for sampling-based uncertainty techniques in object detection. In *Proc. IEEE Int. Conf. Robot. Autom. (ICRA)*, pages 2348–2354, 2019. 1
- [30] Grégoire Montavon, Sebastian Lapuschkin, Alexander Binder, Wojciech Samek, and Klaus-Robert Müller. Explaining nonlinear classification decisions with deep taylor decomposition. *Pattern Recognition*, 65:211–222, 2017. 11
- [31] Paul Novello, Thomas Fel, and David Vigouroux. Making sense of dependence: Efficient black-box explanations using dependence measure. In *Adv. Neural Inform. Process. Syst. (NeurIPS)*, pages 4344–4357, 2022. 5, 6, 7, 8
- [32] Vitali Petsiuk, Abir Das, and Kate Saenko. RISE: Randomized input sampling for explanation of black-box models. In *Brit. Mach. Vis. Conf. (BMVC)*, page 151, 2018. 3
- [33] Vitali Petsiuk, Rajiv Jain, Varun Manjunatha, Vlad I Morariu, Ashutosh Mehra, Vicente Ordonez, and Kate Saenko. Black-box explanation of object detectors via saliency maps. In *IEEE Conf. Comput. Vis. Pattern Recog. (CVPR)*, pages 11443–11452, 2021. 2, 3, 5, 6, 7, 8, 12
- [34] Alec Radford, Jong Wook Kim, Chris Hallacy, Aditya Ramesh, Gabriel Goh, Sandhini Agarwal, Girish Sastry, Amanda Askell, Pamela Mishkin, Jack Clark, et al. Learning transferable visual models from natural language supervision. In *Int. Conf. Mach. Learn. (ICML)*, pages 8748–8763, 2021. 1, 2
- [35] Joseph Redmon and Ali Farhadi. YOLOv3: An incremental improvement. *arXiv preprint arXiv:1804.02767*, 2018. 12
- [36] Shaoqing Ren, Kaiming He, Ross Girshick, and Jian Sun. Faster R-CNN: Towards real-time object detection with region proposal networks. *IEEE Trans. Pattern Anal. Mach. Intell.*, 39(6):1137–1149, 2016. 2
- [37] M Scott, Lee Su-In, et al. A unified approach to interpreting model predictions. In *Adv. Neural Inform. Process. Syst. (NeurIPS)*, pages 4765–4774, 2017. 3
- [38] Ramprasaath R Selvaraju, Michael Cogswell, Abhishek Das, Ramakrishna Vedantam, Devi Parikh, and Dhruv Batra. Grad-CAM: visual explanations from deep networks via gradient-based localization. *Int. J. Comput. Vis.*, 128:336–359, 2020. 3, 5, 6, 7, 8, 12
- [39] Mukund Sundararajan, Ankur Taly, and Qiqi Yan. Axiomatic attribution for deep networks. In *Int. Conf. Mach. Learn. (ICML)*, pages 3319–3328, 2017. 3, 11
- [40] Zhi Tian, Chunhua Shen, Hao Chen, and Tong He. FCOS: A simple and strong anchor-free object detector. *IEEE Trans. Pattern Anal. Mach. Intell.*, 44(4):1922–1933, 2020. 2, 12
- [41] Ashish Vaswani, Noam Shazeer, Niki Parmar, Jakob Uszkoreit, Llion Jones, Aidan N Gomez, Łukasz Kaiser, and Illia Polosukhin. Attention is all you need. In *Adv. Neural Inform. Process. Syst. (NeurIPS)*, pages 5998–6008, 2017. 2
- [42] Chien-Yao Wang, Alexey Bochkovskiy, and Hong-Yuan Mark Liao. YOLOv7: Trainable bag-of-freebies sets new state-of-the-art for real-time object detectors. In *IEEE Conf. Comput. Vis. Pattern Recog. (CVPR)*, pages 7464–7475, 2023. 2
- [43] Haofan Wang, Zifan Wang, Mengnan Du, Fan Yang, Zijian Zhang, Sirui Ding, Piotr Mardziel, and Xia Hu. Score-cam: Score-weighted visual explanations for convolutional neural networks. In *Proceedings of the IEEE/CVF conference on computer vision and pattern recognition workshops*, pages 24–25, 2020. 5
- [44] Xingxing Wei, Siyuan Liang, Ning Chen, and Xiaochun Cao. Transferable adversarial attacks for image and video object detection. In *IJCAI*, pages 954–960, 2019. 1
- [45] Licheng Wen, Xuemeng Yang, Daocheng Fu, Xiaofeng Wang, Pinlong Cai, Xin Li, MA Tao, Yingxuan Li, XU Linran, Dengke Shang, et al. On the road with gpt-4v (ision): Explorations of utilizing visual-language model as autonomous driving agent. In *ICLR 2024 Workshop on Large Language Model (LLM) Agents*, 2024. 1
- [46] Samuel Wilson, Tobias Fischer, Feras Dayoub, Dimity Miller, and Niko Sünderhauf. Safe: Sensitivity-aware features for out-of-distribution object detection. In *Int. Conf. Comput. Vis. (ICCV)*, pages 23565–23576, 2023. 1
- [47] Junfeng Wu, Yi Jiang, Qihao Liu, Zehuan Yuan, Xiang Bai, and Song Bai. General object foundation model for images and videos at scale. In *IEEE Conf. Comput. Vis. Pattern Recog. (CVPR)*, pages 3783–3795, 2024. 1
- [48] Jianzong Wu, Xiangtai Li, Shilin Xu, Haobo Yuan, Henghui Ding, Yibo Yang, Xia Li, Jiangning Zhang, Yunhai Tong, Xudong Jiang, et al. Towards open vocabulary learning: A survey. *IEEE Trans. Pattern Anal. Mach. Intell.*, 2024. 2
- [49] Bin Xiao, Haiping Wu, Weijian Xu, Xiyang Dai, Houdong Hu, Yumao Lu, Michael Zeng, Ce Liu, and Lu Yuan. Florence-2: Advancing a unified representation for a variety of vision tasks. In *IEEE Conf. Comput. Vis. Pattern Recog. (CVPR)*, pages 4818–4829, 2024. 1, 2, 5, 6
- [50] Toshinori Yamauchi. Spatial Sensitive Grad-CAM++: Improved visual explanation for object detectors via weighted combination of gradient map. In *CVPR Workshop*, pages 8164–8168, 2024. 3, 5, 6, 7, 8
- [51] Lewei Yao, Renjie Pi, Jianhua Han, Xiaodan Liang, Hang Xu, Wei Zhang, Zhenguo Li, and Dan Xu. Detclipv3: Towards versatile generative open-vocabulary object detection. In *IEEE Conf. Comput. Vis. Pattern Recog. (CVPR)*, pages 27391–27401, 2024. 1
- [52] Yuhang Zang, Wei Li, Jun Han, Kaiyang Zhou, and Chen Change Loy. Contextual object detection with multimodal large language models. *Int. J. Comput. Vis.*, pages 1–19, 2024. 1

- [53] Jianming Zhang, Sarah Adel Bargal, Zhe Lin, Jonathan Brandt, Xiaohui Shen, and Stan Sclaroff. Top-down neural attention by excitation backprop. *Int. J. Comput. Vis.*, 126(10):1084–1102, 2018. 5
- [54] Chenyang Zhao, Janet H Hsiao, and Antoni B Chan. Gradient-based instance-specific visual explanations for object specification and object discrimination. *IEEE Trans. Pattern Anal. Mach. Intell.*, 2024. 2, 3, 5, 6, 7, 8, 12
- [55] Chenyang Zhao, Kun Wang, Xingyu Zeng, Rui Zhao, and Antoni B Chan. Gradient-based visual explanation for transformer-based clip. In *Int. Conf. Mach. Learn. (ICML)*, pages 61072–61091, 2024. 1
- [56] Xueyan Zou, Zi-Yi Dou, Jianwei Yang, Zhe Gan, Linjie Li, Chunyuan Li, Xiyang Dai, Harkirat Behl, Jianfeng Wang, Lu Yuan, et al. Generalized decoding for pixel, image, and language. In *IEEE Conf. Comput. Vis. Pattern Recog. (CVPR)*, pages 15116–15127, 2023. 1
- [57] Zhengxia Zou, Keyan Chen, Zhenwei Shi, Yuhong Guo, and Jieping Ye. Object detection in 20 years: A survey. *Proceedings of the IEEE*, 111(3):257–276, 2023. 1

Appendix

A. Proof of Theorem 1 (Submodular Properties)

Proof. Consider two sub-sets S_A and S_B in set V , where $S_A \subseteq S_B \subseteq V$. Given an element α , where $\alpha = V \setminus S_B$. Let $\alpha = V \setminus S_B$ represent an element not in S_B . For the function $\mathcal{F}(\cdot)$ to satisfy the submodular property, the following necessary and sufficient conditions must hold diminishing returns,

$$\mathcal{F}(S_A \cup \{\alpha\}) - \mathcal{F}(S_A) \geq \mathcal{F}(S_B \cup \{\alpha\}) - \mathcal{F}(S_B), \quad (6)$$

and monotonic non-negative, $\mathcal{F}(S_A \cup \{\alpha\}) - \mathcal{F}(S) \geq 0$.

For Clue score (Eq. 2), let $f_{\text{cls}}(S) = \mathbf{s}_c$, $f_{\text{reg}}(S) = \mathbf{b}$, assuming that f_{cls} and $f_{\text{reg}}(S)$ is differentiable in S , the individual element α of the collection division is relatively small, according to the Taylor decomposition [30], we can locally approximate $f_{\text{cls}}(S_A + \alpha) = f_{\text{cls}}(S_A) + \nabla f_{\text{cls}}(S_A) \cdot \alpha$, and $f_{\text{reg}}(S_A + \alpha) = f_{\text{reg}}(S_A) + \nabla f_{\text{reg}}(S_A) \cdot \alpha$. Since object detection can output many candidate boxes, we can regard the model output with added sub-elements as incremental output, that is, $f_{\text{cls}}(S_A + \alpha) = \mathbf{s}_c + \nabla f_{\text{cls}}(S_A) \cdot \alpha = \mathbf{s}_c + \mathbf{s}_c^*$, $f_{\text{reg}}(S_A + \alpha) = \mathbf{b} + \nabla f_{\text{reg}}(S_A) \cdot \alpha = \mathbf{b} + \mathbf{b}^*$. Assuming that the searched α

is valid, i.e., $\nabla f_{\text{reg}} > 0$ and $\nabla f_{\text{cls}} > 0$. Thus:

$$\begin{aligned} & s_{\text{clue}}(S_A + \alpha, \mathbf{b}_{\text{target},c}) - s_{\text{clue}}(S_A, \mathbf{b}_{\text{target},c}) \\ &= \max_{\mathbf{b}_i \in f_{\text{reg}}(S_A + \alpha), \mathbf{s}_{c,i} \in f_{\text{cls}}(S_A + \alpha)} \text{IoU}(\mathbf{b}_{\text{target}}, \mathbf{b}_i) \cdot s_{c,i} \\ &\quad - \max_{\mathbf{b}_i \in f_{\text{reg}}(S_A), \mathbf{s}_{c,i} \in f_{\text{cls}}(S_A)} \text{IoU}(\mathbf{b}_{\text{target}}, \mathbf{b}_i) \cdot s_{c,i} \\ &= \max(s_{\text{clue}}(S_A, \mathbf{b}_{\text{target},c}), \max_{\mathbf{b}_i \in \mathbf{b}^*, \mathbf{s}_{c,i} \in \mathbf{s}_c^*} \text{IoU}(\mathbf{b}_{\text{target}}, \mathbf{b}_i) \cdot s_{c,i}) \\ &\quad - s_{\text{clue}}(S_A, \mathbf{b}_{\text{target},c}) \\ &= \max(0, \max_{\mathbf{b}_i \in \mathbf{b}^*, \mathbf{s}_{c,i} \in \mathbf{s}_c^*} \nabla f_{\text{reg}}(S_A) \cdot \nabla f_{\text{cls}}(S_A) \cdot \alpha^2) \\ &\geq 0, \end{aligned} \quad (7)$$

the clue score satisfies the monotonic non-negative property in the process of maximizing the marginal effect. Since $S_A \subseteq S_B \subseteq V$, for the model’s candidate boxes, $f_{\text{reg}}(S_B) > f_{\text{reg}}(S_A)$, then the range of the gain candidate box \mathbf{b}_A^* that can be generated is $f_{\text{reg}}(V) - f_{\text{reg}}(S_A)$. After introducing the new element α , a new candidate box with a gain $\mathbf{b}_A^* > \mathbf{b}_B^*$, closer to the target, can be generated. If both S_A and S_B contain positive subsets, then $\nabla f_{\text{cls}}(S_B)$ will become less severe or even disappear [39], thus, $\nabla f_{\text{cls}}(S_A) > \nabla f_{\text{cls}}(S_B)$. So we have:

$$\begin{aligned} & \max_{\mathbf{b}_i \in \mathbf{b}_A^*, \mathbf{s}_{c,i} \in \mathbf{s}_c^*} \nabla f_{\text{reg}}(S_A) \cdot \nabla f_{\text{cls}}(S_A) \cdot \alpha^2 > \\ & \max_{\mathbf{b}_i \in \mathbf{b}_B^*, \mathbf{s}_{c,i} \in \mathbf{s}_c^*} \nabla f_{\text{reg}}(S_B) \cdot \nabla f_{\text{cls}}(S_B) \cdot \alpha^2, \end{aligned} \quad (8)$$

combining Eq. 7, we have:

$$\begin{aligned} & s_{\text{clue}}(S_A + \alpha, \mathbf{b}_{\text{target},c}) - s_{\text{clue}}(S_A, \mathbf{b}_{\text{target},c}) > \\ & s_{\text{clue}}(S_B + \alpha, \mathbf{b}_{\text{target},c}) - s_{\text{clue}}(S_B, \mathbf{b}_{\text{target},c}). \end{aligned} \quad (9)$$

Similar, for Collaboration score (Eq. 3), according to the Taylor decomposition [30], we can locally approximate $f_{\text{cls}}(V \setminus (S_A + \alpha)) = f_{\text{cls}}(V \setminus S_A) - \nabla f_{\text{cls}}(V \setminus S_A) \cdot \alpha$ and $f_{\text{reg}}(V \setminus (S_A + \alpha)) = f_{\text{reg}}(V \setminus S_A) - \nabla f_{\text{reg}}(V \setminus S_A) \cdot \alpha$. The model output can be viewed as a negative gain process, i.e., $f_{\text{reg}}(V \setminus (S_A + \alpha)) = \mathbf{b} - \mathbf{b}^*$. Assuming that the searched α is valid, i.e., $\nabla f_{\text{reg}} > 0$ and $\nabla f_{\text{cls}} > 0$. We have:

$$\begin{aligned} & s_{\text{colla.}}(S_A + \alpha, \mathbf{b}_{\text{target},c}) - s_{\text{colla.}}(S_A, \mathbf{b}_{\text{target},c}) \\ &= \max_{\mathbf{b}_i \in f_{\text{reg}}(V \setminus S_A), \mathbf{s}_{c,i} \in f_{\text{cls}}(V \setminus S_A)} \text{IoU}(\mathbf{b}_{\text{target}}, \mathbf{b}_i) \cdot s_{c,i} \\ &\quad - \max_{\mathbf{b}_i \in f_{\text{reg}}(V \setminus (S_A + \alpha)), \mathbf{s}_{c,i} \in f_{\text{cls}}(V \setminus (S_A + \alpha))} \text{IoU}(\mathbf{b}_{\text{target}}, \mathbf{b}_i) \cdot s_{c,i} \\ &= 1 - s_{\text{colla.}}(S_A, \mathbf{b}_{\text{target},c}) \\ &\quad - \min(1 - s_{\text{colla.}}(S_A, \mathbf{b}_{\text{target},c}), \max_{\mathbf{b}_i \in \mathbf{b}^*, \mathbf{s}_{c,i} \in \mathbf{s}_c^*} \text{IoU}(\mathbf{b}_{\text{target}}, \mathbf{b}_i) \cdot s_{c,i}) \\ &= \max(0, \max_{\mathbf{b}_i \in \mathbf{b}^*, \mathbf{s}_{c,i} \in \mathbf{s}_c^*} \nabla f_{\text{reg}}(V \setminus S_A) \cdot \nabla f_{\text{cls}}(V \setminus S_A) \cdot \alpha^2) \\ &\geq 0, \end{aligned} \quad (10)$$

Table 7. Evaluation of faithfulness metrics (Deletion, Insertion AUC scores, and average highest score) and location metrics (Point Game and Energy Point Game) on the MS-COCO validation set for correctly detected or grounded samples using traditional object detectors.

Detectors	Methods	Faithfulness Metrics						Location Metric
		Ins. (\uparrow)	Del. (\downarrow)	Ins. (class) (\uparrow)	Del. (class) (\downarrow)	Ins. (IoU) (\uparrow)	Del. (IoU) (\downarrow)	Point Game (\uparrow)
Mask R-CNN [13] (Two-stage)	Grad-CAM [38]	0.2657	0.2114	0.3746	0.3122	0.5348	0.4954	0.5554
	D-RISE [33]	0.6756	0.0814	0.7666	0.1570	0.8396	0.2987	0.8996
	ODAM [54]	0.6067	0.0787	0.7218	0.1860	0.7890	0.3188	0.9934
	Ours	0.7991	0.0489	0.8678	0.1065	0.8968	0.2841	0.9987
YOLO V3 [35] (One-stage)	Grad-CAM [38]	0.6283	0.2867	0.7961	0.4573	0.7271	0.5234	0.7268
	D-RISE [33]	0.7524	0.1889	0.8747	0.3629	0.8213	0.4587	0.8816
	ODAM [54]	0.7329	0.2766	0.8943	0.4707	0.7936	0.5283	0.9838
	Ours	0.8674	0.1407	0.9490	0.3008	0.8984	0.3814	0.9900
FCOS [40] (One-stage)	Grad-CAM [38]	0.2742	0.1417	0.3439	0.1845	0.6858	0.6176	0.5249
	D-RISE [33]	0.4421	0.0570	0.4968	0.1078	0.8578	0.3729	0.9193
	ODAM [54]	0.4266	0.0497	0.4742	0.0853	0.8713	0.4212	0.9935
	Ours	0.5746	0.0414	0.6301	0.0815	0.8900	0.3698	0.9980
SSD [28] (One-stage)	Grad-CAM [38]	0.3869	0.1466	0.4977	0.2022	0.6796	0.5366	0.7700
	D-RISE [33]	0.4882	0.0616	0.5722	0.0979	0.7852	0.4497	0.9243
	ODAM [54]	0.5117	0.0913	0.6072	0.1416	0.7900	0.4801	0.9778
	Ours	0.6891	0.0483	0.7594	0.0835	0.8700	0.4366	0.9941

the collaboration score satisfies the monotonic non-negative property in the process of maximizing the marginal effect. Since $S_A \subseteq S_B \subseteq V$, more candidate boxes will be deleted, thus, $\mathbf{b}_A^* > \mathbf{b}_B^*$, and $\nabla f_{\text{reg}}(V \setminus S_A) > \nabla f_{\text{reg}}(V \setminus S_B)$. Since only a small number of candidate boxes \mathbf{b}^* are removed, $\nabla f_{\text{cls}}(S_A) \cdot \alpha$ can be regarded as a tiny constant and can be ignored. Combining Eq. 10, we have:

$$\begin{aligned} s_{\text{colla.}}(S_A + \alpha, \mathbf{b}_{\text{target},c}) - s_{\text{colla.}}(S_A, \mathbf{b}_{\text{target},c}) > \\ s_{\text{colla.}}(S_B + \alpha, \mathbf{b}_{\text{target},c}) - s_{\text{colla.}}(S_B, \mathbf{b}_{\text{target},c}). \end{aligned} \quad (11)$$

We can prove that both the Clue Score and Collaboration Score satisfy submodularity under certain conditions. Since any linear combination of submodular functions is itself submodular [9], we have:

$$\mathcal{F}(S_A \cup \{\alpha\}) - \mathcal{F}(S_A) \geq \mathcal{F}(S_B \cup \{\alpha\}) - \mathcal{F}(S_B), \quad (12)$$

and we can prove that Eq. 4 satisfies the submodular properties. \square

From the above derivation, we find that the gain or negative gain condition of bounding boxes \mathbf{b}^* is critical for satisfying submodularity. Thus, the detection model f , which can return relevant confidence candidate boxes for any combination of input sub-regions, is theoretically guaranteed to meet the required boundaries. Most detection models fulfill this condition by not filtering out low-confidence candidate boxes. However, multimodal large language model-based detection models, which may not directly output candidate boxes or confidence scores, do not fully satisfy these assumptions. This highlights room for improvement in explaining the results of such models.

B. Faithfulness in Traditional Detectors

We also validated the effectiveness of our interpretation method on traditional object detectors, including the two-stage detector Mask R-CNN (ResNet-50 backbone with Feature Pyramid Networks) [13] and the one-stage detectors YOLO v3 (DarkNet-53 backbone) [35], FCOS (ResNet-50 backbone with Feature Pyramid Networks) [40], and SSD [28]. We use the pre-trained models provided by MMDetection 3.3.0⁵ for interpretation. Following the evaluation settings of D-RISE [33] and ODAM [54], we selected samples for interpretation that were correctly predicted by the model with high confidence and precise localization.

Table 7 presents the results. We observe that, when considering both location and classification faithfulness metrics, D-RISE emphasizes location information more than ODAM, resulting in better performance in this aspect. In contrast, ODAM demonstrates higher faithfulness to classification scores on certain detectors, such as SSD and YOLO v3. Notably, ODAM outperforms D-RISE in the location metric Point Game. While ODAM and D-RISE have specific advantages across different metrics and models, our method consistently achieves state-of-the-art results across all models and metrics. On Mask R-CNN, our method outperforms D-RISE by 18.3% in Insertion and 31.7% in ODAM, as well as by 39.9% and 37.9% in Deletion. On YOLO V3, our method outperforms D-RISE by 15.3% in Insertion and 18.4% in ODAM and by 25.5% and 49.1% in Deletion. On FCOS, our method surpasses D-RISE by 30.0% in Insertion and 34.7% in ODAM, and by 27.4% and

⁵<https://github.com/open-mmlab/mmdetection>

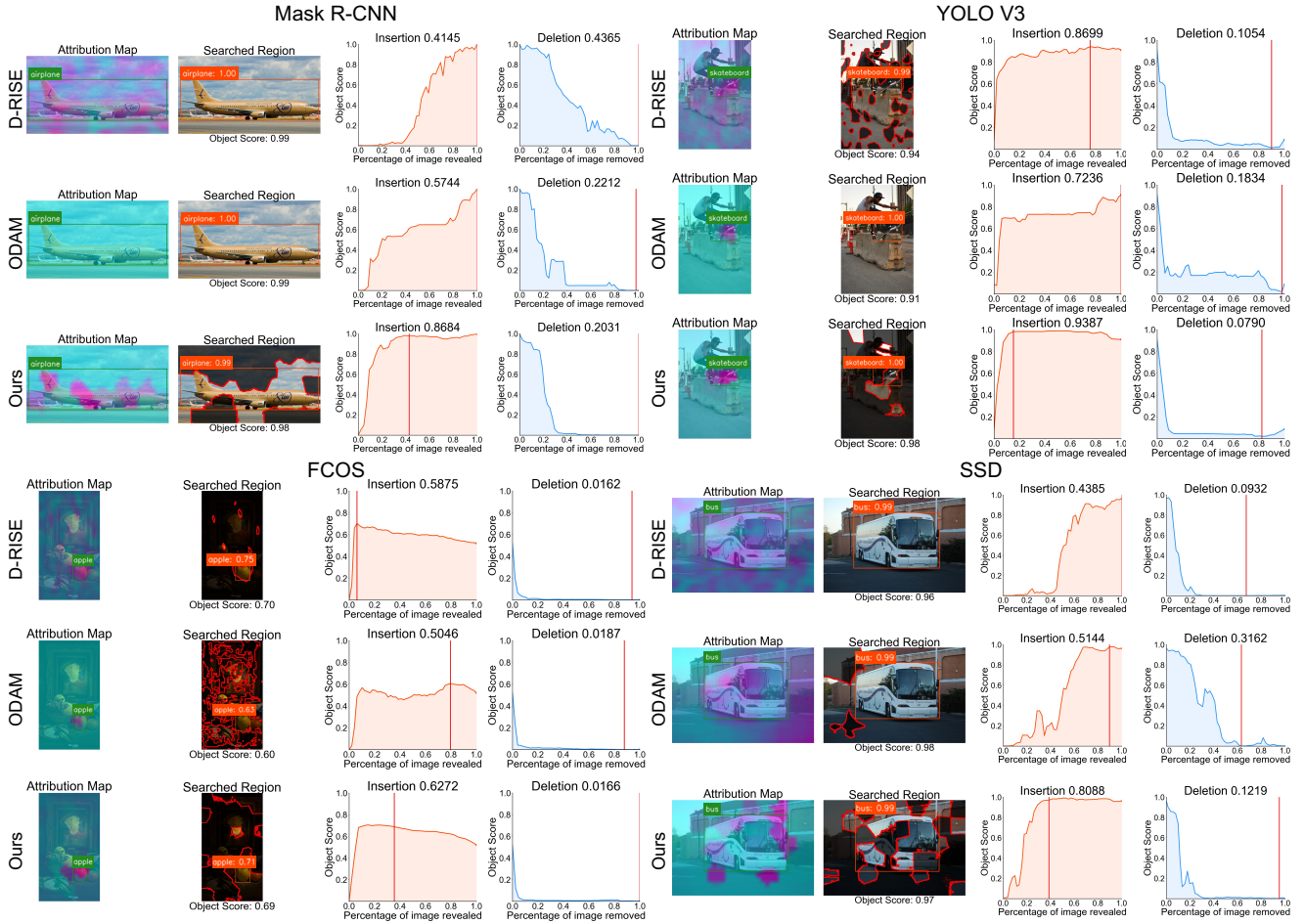


Figure 9. Visualization results of four object detectors for interpreting object detection task on the MS COCO dataset.

16.7% in Deletion. On SSD, our method outperforms D-RISE by 41.2% in Insertion and 17.7% in ODAM, and by 21.6% and 47.1% in Deletion.

From the above results, we found that our method remains highly interpretable even on traditional object detection models, demonstrating its versatility in explaining both modern multimodal foundation models and traditional smaller detectors. Figure 9 presents the visualization results, demonstrating that our method maintains high faithfulness in explaining traditional detectors.

C. Semantic Interpretations

We apply our interpretation method to the visual grounding task using Grounding DINO, focusing on explaining the same location corresponding to different text expressions. As shown in Figure 10, although the important regions are similar when grounding the same object with different texts, the saliency map reveals distinct differences. For the interpretation of the text ‘blue guy’, the person wearing white clothes contributes less than the background region. In con-

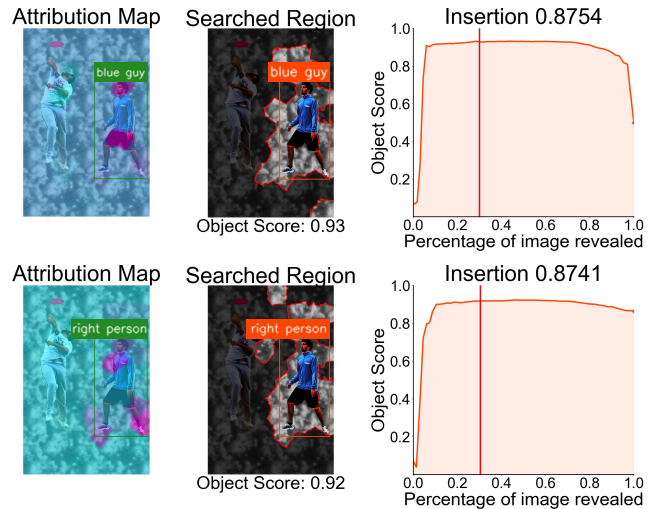


Figure 10. Interpretation of the same instance with different text expressions.

trast, the interpretation of the ‘right person’ highlights only the correct object.

D. Limitation and Discussion

The main limitation of our method is that finer sparse sub-regions enhance explanation faithfulness but significantly increase computation time. Notably, important regions are primarily concentrated around objects. Future work should explore more efficient search methods to improve inference speed while maintaining explanation faithfulness. Additionally, further exploration of sparse approaches could yield promising advancements.

Our method primarily focuses on interpretable attribution at the input level of the model. There remains significant potential for attributing internal parameters, particularly in transformer-based models. This approach could extend to explaining additional tasks, such as instance segmentation. Future research could explore improving models based on this mechanism by identifying and correcting problematic parameters.